# Supplementary Materials for Charge balance strategy for stable QLEDs: *p*-type doping design in quantum dot shells

Yang Huang[1, #], Yangzhi Tan[1, 2, #], Zhongyuan Guan[1], Yiguo Xu[3], Lars Samuelson[1], Kai Wang[1, †], and Xiao Wei Sun[1, †]

[1]Institute of Nanoscience and Applications, and Department of Electrical and Electronic Engineering, Southern University of Science and Technology, Shenzhen 518055, China

[2]Department of Electrical and Electronic Engineering, The University of Hong Kong, Pokfulam Road, Hong Kong 999077, China

[3]Institute of Major Scientific Facilities for New Materials and Academy for Advanced Interdisciplinary Studies, Southern University of Science and Technology, Shenzhen 518055, China

**Density functional theory calculations**

All density functional theory (DFT) calculations were performed using the Vienna *Ab Initio* Simulation Package (VASP) with the projector augmented wave (PAW) method under the generalized-gradient approximation (GGA)[1-3]. A plane-wave energy cutoff of 300 eV was employed for geometry optimization and static calculations. The Brillouin zone was sampled using the Monkhorst-Pack scheme[4] with a Γ-centered *k*-mesh for quantum dot systems. Structural relaxations of both atomic positions and cell parameters were conducted until residual forces on all atoms fell below 0.02 eV/Å.

The QDs were constructed by carving spherical clusters from optimized bulk lattices, with uncompensated surface dangling bonds passivated by pseudo-hydrogen atoms[5, 6]. A 12 Å vacuum layer was introduced to eliminate inter-QD interactions. For ZnS QDs, S and Zn surface atoms were saturated with fictitious hydrogen atoms carrying charges of 0.5*e* and 1.5*e*, respectively, while for InP QDs, P and In atoms were passivated with hydrogen atoms of charges 0.75*e* and 1.25*e*. Five ZnS QD sizes were modeled (diameters: 1.6, 1.8, 2.0, 2.2, and 2.4 nm; atom counts: 163, 247, 291, 453, and 564) and four InP QD sizes were studied (diameters: 1.96, 2.24, 2.40, and 2.76 nm; atom counts: 247, 351, 453, and 684). For comparative defect analysis, a 216-atom ZnS supercell was also constructed. To address the GGA-induced underestimation of bandgaps, single-shot HSE06 hybrid functional calculations[7] were performed on GGA-relaxed structures. The exact exchange fraction (AEXX) was set to 0.3, yielding bulk bandgaps of 3.49 eV (ZnS) and 1.41 eV (InP), consistent with experimental values.

The defect formation energy, $\Delta H_f(\alpha, q)$, is defined as[8–10]:

$$\Delta H_f(\alpha, q) = E(\alpha, q) - E(\text{host}) + \Sigma n_i[\mu_i + E(i)] + q[E_F + \varepsilon_{\text{VBM}}(\text{host})] + E_{corr}$$

where $E(\alpha, q)$ and $E(\text{host})$ denote the total energies of the defective and pristine supercells, respectively. $n_i$ represents the number of atoms of species $i$ added ($n_i < 0$) or removed ($n_i > 0$), $\mu_i$ is the atomic chemical potential (approximated as $\mu_i = 0$ for simplicity), $E_F$ spans from the valence band maximum (VBM) to the conduction band minimum (CBM), and $E_{corr}$ corrects finite-size electrostatic errors arising from periodic boundary conditions. The defect transition energy level $\varepsilon(q/q')$, which is the Fermi energy referenced to VBM at which the defect has the same energy at charge states $q$

and $q'$, is given by

$$\varepsilon(q/q') = [\Delta E(\alpha, q) - \Delta E(\alpha, q')]/(q' - q)$$

**Electrical stimulation of QLED**

The electrical simulation were performed by Setfos 5.0. The material parameters including thickness, highest occupied molecular orbital (HOMO), lowest unoccupied molecular orbital (LUMO), work function ($W_F$), electron- and hole-mobility ($\mu_e$ and $\mu_h$), doping type and concentration of different layers used in the simulation were provided in Table S1. For electrical simulation, the $\mu_e$ and $\mu_h$ of each material were set to constant while the Poole-Frenkel effect describing the field-dependent mobility was neglected. A charge drift-diffusion model was employed to simulate the electroluminescence characteristics of the QLEDs.

In constructing our model, we made certain simplifying assumptions to isolate the core research question of this study. Specifically, we assumed identical electron and hole mobilities within the QDs layer and used a fixed, representative *p*-doping concentration for the hole transport and doped-shell layers. To rigorously validate these assumptions and understand their potential impact on our conclusions, we performed extensive additional simulations, with the results compiled and analyzed in Fig. S2. As shown in Fig. S2, the detailed analysis confirms that our main conclusions are robust and are not artifacts of the initial simplifying assumptions. The device simulations

**Table S1.** The parameters used in electrical simulation of QLEDs.

| Layer | Thickness (nm) | HOMO (eV) | LUMO (eV) | WF (eV) | $\mu_e$ ($cm^2 \cdot V^{-1} \cdot s^{-1}$) | $\mu_h$ ($cm^2 \cdot V^{-1} \cdot s^{-1}$) | Doping ($cm^{-3}$) |
|---|---|---|---|---|---|---|---|
| ITO | 100 | / | / | 4.70 | / | / | / |
| PEDOT:PSS [11] | 30 | -5.20 | -2.90 | / | / | $2.6\times10^{-4}$ | *p*-doped ($10^{19}$) |
| TFB[12] | 30 | -5.30 | -2.40 | / | / | $1.0\times10^{-2}$ | / |
| ZnS shell | 2 | -6.41 | -1.67 | / | $1.0\times10^{-3}$ | $1.0\times10^{-3}$ | / |
| ZnS:Na shell | 2 | -6.23 | -1.65 | / | $1.0\times10^{-3}$ | $1.0\times10^{-3}$ | *p*-doped ($10^{19}$) |
| InP core | 2.24 | -5.87 | -2.92 | / | $1.0\times10^{-3}$ | $1.0\times10^{-3}$ | / |
| ZnO NPs[13] | 40 | -7.90 | -4.30 | / | $2.0\times10^{-3}$ | / | / |
| Ag | 100 | / | / | 4.50 | / | / | / |

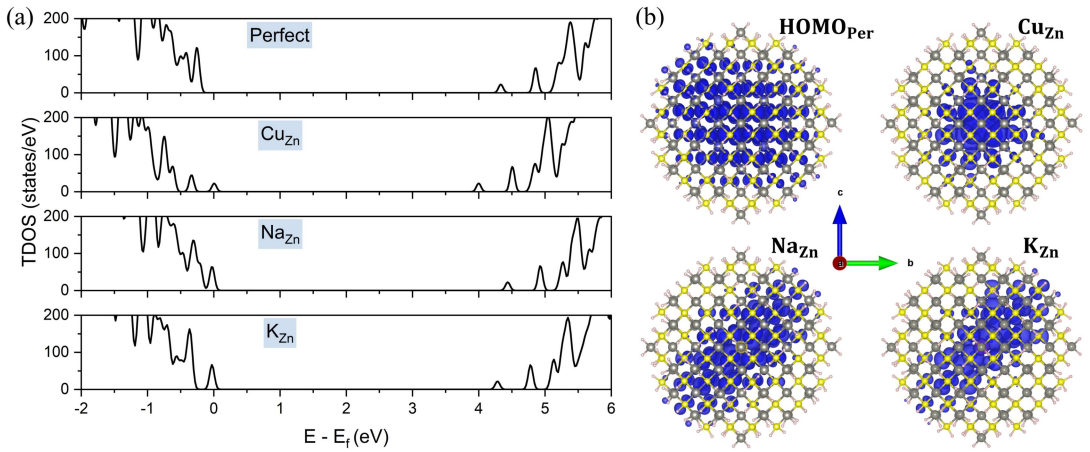



**Fig. S1.** (Color online) (a) Calculated total DOS for a 2.2 nm diameter ZnS QD, both without doping and with doping. (b) Partial charge density distributions of the HOMO, $Cu_{Zn}^{0}$, $Na_{Zn}^{0}$, and $K_{Zn}^{0}$ energy levels in the ZnS QD. The isosurface value is set to 0.0002 |e|/bohr$^3$.

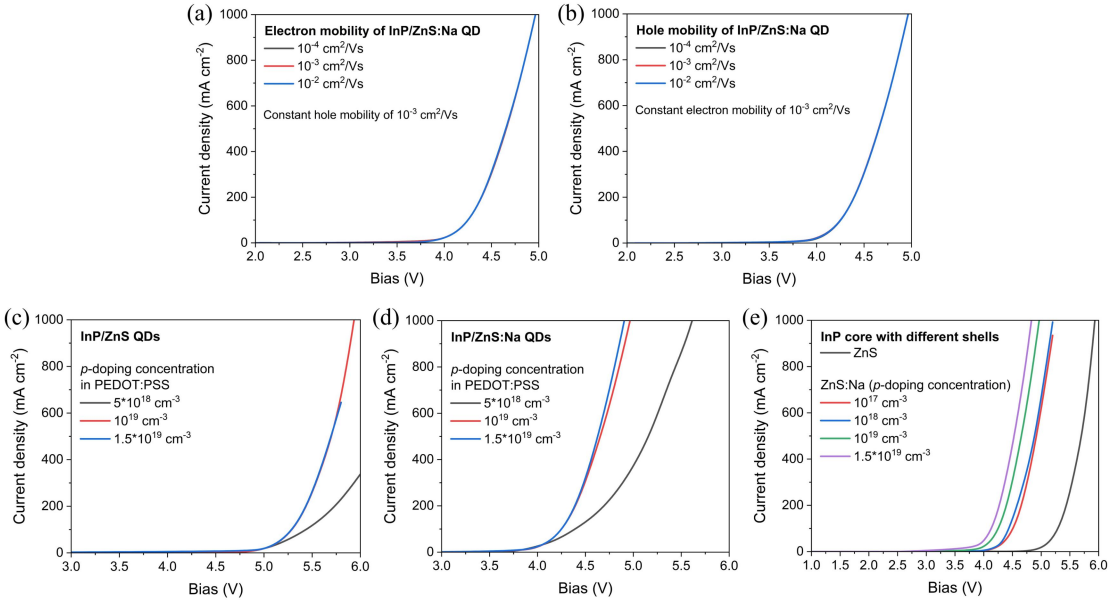



**Fig. S2.** (Color online) Investigation of simulation parameter assumptions. J-V characteristics of an InP/ZnS:Na QLED with varying (a) electron mobility and (b) hole mobility in the QD layer. The constant mobility is fixed at $10^{-3}$ cm$^2$·V$^{-1}$·s$^{-1}$. (c) J-V curves for an InP/ZnS QLED with varying *p*-doping concentrations in the PEDOT:PSS layer. (d) J-V curves for an InP/ZnS:Na QLED (with a fixed shell doping of $10^{19}$ cm$^{-3}$) with varying p-doping concentrations in the PEDOT:PSS layer. (e) J-V curves for InP/ZnS:Na QLEDs with varying *p*-doping concentrations in the ZnS:Na shell, compared to the undoped InP/ZnS device.

clearly demonstrate that the primary mechanism for performance enhancement is the targeted *p*-doping of the QD shell, which directly addresses the critical hole injection bottleneck in the device.

**Investigation of simulation parameter assumptions**

The following simulation results reveal that the device's J-V characteristics, particularly the turn-on voltage, are remarkably insensitive to the electron and hole mobilities in the QD layer. Varying these values over several orders of magnitude (from $10^{-4}$ to $10^{-2}$ $cm^2 \cdot V^{-1} \cdot s^{-1}$) produced negligible changes. This is because in these QLED architectures, the primary bottleneck for current flow, especially near turn-on, is the large energy barrier for charge injection at the transport-layer/QD interfaces. Compared to the energy required to overcome this injection barrier, the rate at which carriers drift across the thin QD layer (governed by mobility) is a secondary effect. Therefore, the injection physics, rather than the intra-layer transport speed, dominates the device's turn-on behavior.

Besides, the model shows that the device's $V_{on}$ is also insensitive to the *p*-doping concentration in the highly conductive PEDOT:PSS layer (Figs. S2(c) and S2(d)). Since PEDOT:PSS already possesses a high carrier concentration (~$10^{19}$ $cm^{-3}$, a reasonable value according to the literature[14–16]), its primary role is to act as an efficient reservoir of holes for the subsequent TFB layer. Further increasing its doping does not alter the main energy barrier at the TFB/QD interface, thus having little effect on the turn-on voltage.

Conversely, the device performance is critically dependent on the *p*-doping concentration of the ZnS:Na shell (Fig. S2(e)). This is the central finding of our work. The undoped ZnS shell is wide-bandgap, presenting a significant potential barrier that impedes hole injection from the TFB into the InP core. *p*-doping introduces acceptor states within the shell's bandgap, effectively creating an electronic pathway for holes. As the doping concentration increases, this pathway becomes more conductive, drastically reducing both the effective injection barrier and the voltage drop across the shell. This allows for efficient hole injection to commence at a much lower overall device bias, leading to the observed systematic reduction in turn-on voltage.

**Table S2.** Site-dependent defect formation energies ($\Delta H^{QD}$) and acceptor levels ($\varepsilon(0/-)$) of Cu, Na, and K substitution in ZnS QDs. Values are summarized as range (average) over D = 1.6-2.4 nm.

| Site | Dopant | $\Delta H^{QD}$ (eV) | $\varepsilon(0/-)$ (eV) | Key implication |
|---|---|---|---|---|
| Core | Cu | 1.87-1.93 (1.90) | 0.85-1.27 (1.05) | Deep acceptor |
| Core | Na | 1.37-1.58 (1.49) | 0.35-0.57 (0.44) | Low formation energy and shallow acceptor |
| Core | K | 2.04-2.20 (2.13) | 0.48-0.72 (0.59) | Larger distortion, deeper than Na |
| Subsurface | Cu | 1.81-2.10 (1.93) | 1.03-1.52 (1.33) | Deep acceptor |
| Subsurface | Na | 0.80-1.47 (1.10) | 0.31-0.49 (0.38) | Shallowest average acceptor |
| Subsurface | K | 0.47-1.08 (0.73) | 0.28-0.84 (0.51) | Low formation energy but less robust ionization |
| Surface | Cu | 1.84-1.96 (1.91) | 0.83-1.73 (1.20) | Deep acceptor |
| Surface | Na | 1.10-1.52 (1.29) | 0.28-0.50 (0.38) | Low formation energy and shallowest average acceptor |
| Surface | K | 1.16-1.56 (1.36) | 0.29-0.59 (0.43) | Slightly deeper than Na |

**Table S3.** Calculated defect formation energies for $X_{Zn}^{0}$ (X = Cu, Na, K, Al, Mn) in ZnS and comparison with experimental evidence. $\Delta H^{bulk}$ and $\Delta H^{QD}$ represent defect formation energies derived from ZnS supercell and ZnS QD models (within 1.6-2.4 nm), respectively.

| Dopant | $\Delta H^{bulk}$ (eV) | $\Delta H^{QD}$ (eV) | Potential theoretical feasibility | Experimental feasibility |
|---|---|---|---|---|
| Cu | 1.79 | 1.87-1.93 | √ | √[17−19] a) |
| Na | 1.23 | 1.37-1.58 | √ | / |
| K | 2.09 | 2.04-2.15 | √ | /b) |
| Al | 0.23 | 0.83-1.25 | √ | √[23] |
| Mn | 0.51 | 0.51-0.53 | √ | √[24, 25] |

**Notes: a)** Cu doping has also been commonly achieved in other II-VI and II-V QDs[20, 21].

**b)** Experimentally, K doping has been demonstrated to be feasible in HgTe and InAs QDs[22].

**Reference**

[1] Kohn W, Sham L J. Self-consistent equations including exchange and correlation effects. **Phys Rev**, 1965, **140**(4A): A1133

[2] Blöchl P E. Projector augmented-wave method. **Phys Rev B**, 1994, **50**(24): 17953

[3] Kresse G, Joubert D. From ultrasoft pseudopotentials to the projector augmented-wave method. **Phys Rev B**, 1999, **59**(3): 1758

[4] Monkhorst H J, Pack J D. Special points for Brillouin-zone integrations. **Phys Rev B**, 1976, **13**(12): 5188

[5] Cho E, Jang H, Lee J, et al. Modeling on the size dependent properties of InP quantum dots: a hybrid functional study. **Nanotechnology**, 2013, **24**(21): 215201

[6] Fu H X, Zunger A. InP quantum dots: Electronic structure, surface effects, and the redshifted emission. **Phys Rev B**, 1997, **56**(3): 1496

[7] Heyd J, Scuseria G E, Ernzerhof M. Hybrid functionals based on a screened Coulomb potential. **J Chem Phys**, 2006, **124**(21): 219906

[8] Freysoldt C, Grabowski B, Hickel T, et al. First-principles calculations for point defects in solids. **Rev Mod Phys**, 2014, **86**(1): 253

[9] Wei S H. Overcoming the doping bottleneck in semiconductors. **Comput Mater Sci**, 2004, **30**(3–4): 337

[10] Huang M L, Zheng Z N, Dai Z X, et al. DASP: Defect and dopant ab-initio simulation package. **J Semicond**, 2022, **43**(4): 042101

[11] Zheng Z, Hu Q, Zhang S Q, et al. A highly efficient non-fullerene organic solar cell with a fill factor over 0.80 enabled by a fine-tuned hole-transporting layer. **Adv Mater**, 2018, **30**(34): 1801801

[12] Yang Y X, Zheng Y, Cao W R, et al. High-efficiency light-emitting devices based on quantum dots with tailored nanostructures. **Nat Photonics**, 2015, **9**(4): 259

[13] Dai X L, Zhang Z X, Jin Y Z, et al. Solution-processed, high-performance light-emitting diodes based on quantum dots. **Nature**, 2014, **515**(7525): 96

[14] Han C, Qiu J, Liu H, et al. Tunable ENZ properties in organic material PEDOT:PSS treated with different solutions. **Opt Mater Express**, 2024, **14**(6): 1631

[15] Wang X, Kyaw A K K, Yin C, et al. Enhancement of thermoelectric performance

of PEDOT:PSS films by post-treatment with a superacid. **RSC Adv**, 2018, **8**(33): 18334

[16] Guo Z, Sato T, Han Y, et al. Band transport evidence in PEDOT:PSS films using broadband optical spectroscopy from terahertz to ultraviolet region. **Commun Mater**, 2024, **5**(1): 26

[17] Panfil Y E, Thompson S M, Chen G, et al. Room-temperature quantum emission from $Cu_{Zn}$-$V_S$ defects in ZnS:Cu colloidal nanocrystals. **ACS Nano**, 2025, **19**(23): 21400

[18] Thompson S M, Şahin C, Yang S, et al. Red emission from copper-vacancy color centers in zinc sulfide colloidal nanocrystals. **ACS Nano**, 2023, **17**: 5963

[19] Bang J, Das S, Yu E-J, et al. Controlled photoinduced electron transfer from InP/ZnS quantum dots through Cu doping: A new prototype for the visible-light photocatalytic hydrogen evolution reaction. **Nano Lett**, 2020, **20**(8): 6263

[20] Srivastava B B, Jana S, Pradhan N. Doping Cu in semiconductor nanocrystals: some old and some new physical insights. **J Am Chem Soc**, 2011, **133**: 1007

[21] Knowles K E, Hartstein K H, Kilburn T B, et al. Luminescent colloidal semiconductor nanocrystals containing copper: synthesis, photophysics, and applications. **Chem Rev**, 2016, **116**: 10820

[22] Mastrippolito D, Cavallo M, Jalali H B, et al. Tuning electronic properties of II-VI and III-V narrow bandgap nanocrystals through exposure to alkali. **Chem Mater**, 2024, **36**: 11669

[23] Koh S, Lee H, Lee T, et al. Enhanced thermal stability of InP quantum dots coated with Al-doped ZnS shell. **J Chem Phys**, 2019, **151**: 144704

[24] Nistor S V, Stefan M, Nistor L C, et al. Incorporation and localization of substitutional $Mn^{2+}$ ions in cubic ZnS quantum dots. **Phys Rev B**, 2010, **81**: 035336

[25] Ang E H, Zeng J, Subramanian G S, et al. Silica-coated Mn-doped ZnS nanocrystals for cancer theranostics. **ACS Appl Nano Mater**, 2020, **3**(3): 3088